HHS Public Access

Author manuscript

Microvasc Res. Author manuscript; available in PMC 2020 January 01.

Published in final edited form as:

Microvasc Res. 2019 January ; 121: 37–45. doi:10.1016/j.mvr.2018.09.003.

Evaluating changes of blood flow in retina, choroid, and outer choroid in rats in response to elevated intraocular pressure by 1300nm swept-source OCT

Jingjiang Xu[1], **Yuandong Li**[1], **Song Shaozhen**[1], **William Cepurna**[2], **John Morrison**[2], and **Ruikang K. Wang**[1,3,*]

[1]University of Washington, Department of Bioengineering, Seattle, WA 98195, USA

[2]Casey Eye Institute, Oregon Health & Science University, Portland, OR 97239, USA

[3]University of Washington, Department of Ophthalmology, Seattle, WA 98104, USA

Abstract

We report the development of a 1300nm swept-source optical coherence tomography (SS-OCT) system specifically designed to perform OCT imaging and optical microangiography (OMAG) in rat eyes *in vivo* and its use in evaluating the effects of intraocular pressure (IOP) elevation on ocular circulation. The swept laser is operated in single longitude mode with a 90 nm bandwidth centered at 1300 nm and 200 kHz A-line rate, providing remarkable sensitivity fall-off performance along the imaging depth, a larger field of view of 2.5×2.5 mm^2 (approximately 35°), and more time-efficient imaging acquisition. The advantage of the SS-OCT/OMAG is highlighted by an increased imaging depth of the entire posterior thickness of optic nerve head (ONH) and its surrounding vascular anatomy, to include, for the first time *in vivo*, the vasculature at the scleral opening, allowing visualization of the circle of Zinn-Haller and posterior ciliary arteries (PCAs). Furthermore, the capillary-level resolution angiograms achieved at the retinal and choroidal layers over a larger field of view enable a significantly improved quantification of the response of vascular area density (VAD) to elevated IOP. The results indicate that reduction in perfusion of the choroid in response to elevated IOP is delayed compared to that seen in the retina; while choroidal VAD doesn't reach 50% of baseline until ~70 mmHg, the same effect is seen for the retinal VAD at ~60 mmHg. The superior image quality offered by SS-OCT may allow more comprehensive investigation of IOP-related ocular perfusion changes and their pathological roles in glaucomatous optic nerve damage.

Keywords

Optical coherence tomography; optical microangiography; swept source OCT; glaucoma; intraocular pressure; ocular perfusion; circle of Zinn-Haller; optic nerve head

* wangrk@uw.edu.

1. Introduction

The posterior segment microvasculature of the eye, including retinal and choroidal vessels, and arterial blood supply to the optic nerve head (ONH), is critical to maintain normal vision. The blood perfusion within them is known to be affected by elevated intraocular pressure (IOP), a major risk factor for glaucoma [1-3]. However, the mechanisms that underlie vascular responses to IOP and how these contribute to glaucomatous optic nerve damage are not fully understood [4]. Therefore, the ability to visualize detailed vascular networks in these structures and accurately evaluate their response to changes in IOP are important for both pathophysiology and patient care in glaucoma.

Optical coherence tomography (OCT) is a label-free, non-contact, fast and non-invasive imaging technique that can achieve depth-resolved imaging of tissue structure by using white light Michelson interferometry [5,6]. This imaging modality is an established tool in ophthalmic clinics as well as in glaucoma experimental research for detecting structural changes in the retinal tissue in response to increased IOP and glaucoma progression. As an important extension of OCT, OCT-based angiography (OCTA) enables three-dimensional (3-D) visualization of the vascular networks in living subjects by analyzing the dynamic signals generated by moving red blood cells in perfused blood vessels [7-10]. In previous studies, we have used our unique OCTA algorithm, optical microangiography (OMAG) [11,12], adapted to a spectral domain OCT (SD-OCT) system in rats, to evaluate the effect of elevated IOP on retinal, choroidal and ONH perfusion [13,14]. The results have nicely documented the capability of SD-OCT/OMAG to image the structural and vascular anatomy of the ONH and the adjacent retina and choroid and have quantitatively demonstrated the effects of IOP elevation on capillary filling in these tissues [15].

However, in SD-OCT, spectral resolution is fundamentally limited by the resolving power of the optical grating and the pixel dimensions of the line-scan camera, resulting in significant sensitivity drop-off at deeper axial positions [16,17]. Due to this limitation, the structural and vascular anatomy of the entire thickness of the ONH was not optimally visualized [13], limiting our ability to view the arterial blood supply to the ONH at the scleral canal opening and its response to changing IOP. For the same reason, the blood perfusion map at the choroidal layer has a relatively low signal-to-noise ratio (SNR), which may create uncertainty when quantifying choroid vessel filling. Further limitations include the small field-of-view (1×1 mm^2) [13] of imaging, which is a result of the compromised ability of the SD-OCT system in terms of A-line speed and data acquisition efficiency.

In addition to SD-OCT, another rapidly developing Fourier-domain technique, swept-source OCT (SS-OCT), employs a wavelength-scanning light source and sequentially acquires the spectral interferogram by photodetectors and digitizers [18,19]. Such a working principle offers several advantages in imaging the rat eye *in vivo*. First, the swept laser can operate in a single longitudinal mode with an extremely narrow instantaneous linewidth, providing a remarkable performance with minimal sensitivity fall-off along the axial imaging depth. Second, with a simple and compact configuration of fiber-based dual balanced photo-receivers, it can improve the signal to noise ratio of SS-OCT detection through cancelling the common mode noise, avoiding common-path artifacts, the grating loss and the laborious

alignment of the bulky spectrometer required by the SD-OCT system. Lastly, it offers a faster imaging speed, enabling enough sampling points for a long imaging range and wide field of view (FOV) within a short image acquisition time. With SS-OCT, the imaging speed has been recently reported to improve from 100s kHz [20-22] to 10s MHz [23-29], and the imaging range has been extended from 10s cm to a meter range with an unprecedented FOV (>100s cm^2) [30,31]. These advantages together should help us image the entire thickness of the retina and choroid, which could be important for investigating the response of choroidal perfusion to changes in IOP.

In this study, we demonstrate the use of SS-OCT to perform *in vivo* OCT/OMAG imaging of the posterior structure and vasculature in the rat eye, including the morphology of the entire thickness of the ONH and the arterial blood perfusion at the scleral opening. With this increased imaging depth and large FOV imaging capability, we investigated the effect of acutely elevated IOP on the anatomy and visualization of the vasculature of the retina, choroid, and outer choroid (including sclera and beyond) over a 2.5 × 2.5 mm^2 region (approximately 35° FOV) and quantitatively compared the response of retinal and choroidal vessel filling to different levels of IOP.

2. Material and methods

2.1 SS-OCT system setup

Figure 1(a) shows the schematics of the custom-built SS-OCT system setup for *in vivo* imaging of the rat eye. We employed a compact, custom-made module, which incorporated a broadband swept laser, a Mach-Zehnder interferometer (MZI) and a balance photodetector (BPD) in a small box (~11cm×18cm×4cm). The swept laser has a high-speed A-line rate of 200 kHz with ~90 nm wavelength tuning range centered at 1300 nm. The built-in MZI has 48 mm optical delay, providing an external clock for the digitizer to achieve linear *k*-space sampling of the OCT interferogram. A fiber-based Michelson interferometer was implemented for rat eye imaging, where the light passed through an optical fiber circulator and then split into the reference arm and sample arm by a broadband 50/50 fiber coupler. In the reference arm, the mirror and lens were mounted on a translation stage to adjust the optical delay. A pair of galvanometer scanners was utilized in the sample arm to perform fast and stable XY scanning. A combination of an achromatic lens (75 mm focal length) and an ocular lens (MaxField® Standard 90D, Ocular Instrument) was used to achieve ~ 10 μm lateral resolution for posterior segment imaging. The incident power on the sample arm was ~2 mW, which is safe for rat eyes. To facilitate quick sample positioning, a visible light was coupled in the interferometer through a wavelength division multiplexer (WDM). The sweeping trigger, optical clock and OCT signal from the module were delivered to a 12-bit high-speed digitizer (ATS9360, AlazarTech, Inc.) which has up to a 1.8 G/s sampling rate to achieve a long imaging range. A large dataset from the digitizer was streamed to a host computer (Intel Xeon E5-2660, 64 GB RAM) using an 8-lane PCI Express Gen2 interface. The operations of the SS-OCT system were automatically controlled by a Labview program. Figure 1(b) shows a photograph of the SS-OCT prototype system, which was assembled on a movable cart, easily translatable for use in the tight space of research laboratories. Most parts of the OCT interferometer, including the swept laser, MZI, photodetector, guiding

light, fiber components and reference arm, were built in a standard 19-inch rack box 5.20 inches tall. The sample arm was outside the rack box, where we used a home-made hand-held scanning probe for easy access to the desired tissues for imaging. The fiber cable, as well as the electrical cables for the probe, were packaged in a 1.5-meter cable sleeve. In this study, the scanning probe was mounted in a stable platform for rat eye imaging.

2.2 Animal preparation

All of the animal procedures for this study conformed to the Association for Research in Vision and Ophthalmology (ARVO) Statement for the Use of Animals in Ophthalmic and Vision Research. All animal experimental procedures were approved by the Institutional Animal Care and Use Committee (IACUC) of the University of Washington and conducted in accordance with ARRIVE guidelines. Young (2 months old) brown Norway rats (n=15) with an average body weight of ~ 200 g were used in this study.

Rats were anesthetized with 2%-3% inhalational isoflurane mixed with pure oxygen and active exhaust for waste gas and expired CO_2 removal and positioned in a custom-made stage with multi-dimensional adjustability. The body temperature was maintained at ~38 °C by a heated water blanket. Mean arterial blood pressure (MAP) was monitored non-invasively by CODA tail cuff (Kent Scientific, Torrington, CN, USA) and respiratory rate, pulse and blood oxygen saturation were monitored using a MouseOx plus (Starr Life Sciences, Oakmont, PA, USA) with footpad sensor. Before cannulation, 0.5% proparacaine hydrochloride was instilled for added corneal anesthesia and the pupil was dilated with 1% tropicamide to allow the OCT beam to access the posterior segment. The anterior chamber of the right eye was then entered via the cornea with a 31-gauge needle and cannulated with a 2 cm 0.010” OD polyurethane tube (Instech Labs, Plymouth Meeting, PA USA) connected via a larger tube to a reservoir filled with balanced salt solution and a pressure transducer. The pressure transducer was positioned at the same height as the eye to continuously monitor IOP. The reservoir was suspended by a pulley system and the height adjusted to alter the IOP. This system has previously been shown to reliably produce an IOP equivalent to that indicated by the pressure transducer [32].

The IOP was elevated from 10 mmHg (treated as baseline) to 100 mmHg in 10 mmHg increments, which produced complete obstruction of retinal and choroidal blood flow. IOP was then returned to baseline. At each IOP level, after the height of the reservoir was increased, 20 seconds were given to allow the IOP to stabilize before image acquisition. Saline solution was applied frequently to maintain corneal hydration and clarity throughout the experiment [33].

2.3 Image acquisition and processing

At each IOP level, a 3-D data volume with an *en face* area of 2.5 × 2.5 mm^2 that included the ONH was acquired using the ultrahigh sensitive OMAG step scanning protocol [34], in which 512 A-lines within each B-frame (2-D) and 2560 B-frames in each C-scan (3-D) were performed at a frame rate of 250 frames/sec. These 2560 B-frames were captured at 512 cross-sections with 5 repeated B-frames at each cross-section. The galvo mirrors were driven by a saw tooth waveform in the X direction and a step function in the Y direction. This

scanning pattern allowed a 4 ms time interval between the adjacent B-frames, enabling high flow sensitivity to visualize capillary-level blood vessels. Each 3-D volume took only ~ 10 s to accomplish the data acquisition, which helps minimize motion artifact. The 3-D OMAG data were post-processed using the most recently developed eigen-decomposition (ED)-based OMAG algorithm, which is a method based on multivariate statistical analysis to effectively separate the blood flow from the static tissue with less motion artifact [35,36].

2.4 Quantification of retinal and choroidal blood perfusion

To evaluate the microvascular response to elevated IOP, we first used a semi-automated segmentation software [37] to separate retinal and choroidal layers in the 3D structure OCT scans by identifying the anterior surface of the retina, and the hyper-reflecting retinal pigment epithelium (RPE). Another segmentation line was automatically generated 100 μm posterior to the identified RPE line, that was used to generate a slab that includes all the depth signals below this line, upon which to produce perfusion maps of outer choroidal layer, including sclera. The *en face* maximum intensity projection (MIP) of the retinal vessels was produced by a slab measured from the anterior surface of the retina to ~20 μm anterior to the RPE, and the *en face* MIP for the choroidal vessel quantification was generated from a slab measured ~ 100 μm thickness posterior to the RPE. The resulting segmentation slab was directly applied to 3D blood flow images to obtain a perfusion map for each layer, from which a binary vessel map was generated from the *en face* OCTA image. To quantify the microvascular perfusion at each IOP, we adopted the parameter of vessel area density (VAD), introduced in previous studies, [38,39] to calculate the ratio of area occupied by perfused blood vessels to the total *en face* imaging area. Lastly, we compared the relative change of VAD (to 10mmHg, baseline) at each layer for different IOPs, as well as the relative change of VAD in response to ocular perfusion pressure (OPP). OPP was calculated as the difference between the MAP for each animal and IOP at each level.

2.5 Statistical analysis

The differences between retinal and choroidal vascular density at each IOP level were statistically tested using two-tailed Student *t* tests (n=15) in Microsoft Excel built-in program. $P<0.05$ was considered to be significantly different.

3. Results

3.1 System performance

We first evaluated the system performance prior to *in vivo* imaging. Figure 2(a) shows the spectrum of the swept laser measured by the optical spectrum analyzer (MS9710B, Anritsu), which has a center wavelength of 1300 nm with 90 nm full spectral span. The time waveforms of the laser trigger signals and the swept light from the OCT reference arm were captured by the digitizer (Fig. 2(b)). Although the swept laser performed forward and backward sweeps during each period, only the forward sweep light was used for imaging. The laser trigger had a time period of 5 μs and the swept light occupied 3.5 μs in each period, indicating a high-speed A-line rate of 200 kHz with 70% sweep duty cycle. Then, we generated the system sensitivity fall-off curves by changing the position of the lens and

mirror in the reference arm (Fig. 2(c)). As the digitizer utilized the external clock for linear *k* space data sampling, it was not necessary to apply spectral calibration for the improvement of the point spread function (PSF). The system had an imaging range of 12 mm that was determined by the optical delay of the built-in MZI. The sensitivity of the OCTA system was measured at ~105 dB near the zero-depth position. Due to the extremely narrow instantaneous linewidth of the swept laser, the system maintained high sensitivity (>100 dB) within the 12 mm range. Moreover, as shown by the blue points and curve in Fig. 2(c), the axial resolution was also relatively stable, varying from 13 μm to 16 μm within the 12-mm imaging range.

3.2 In vivo OCTA imaging of the rat eye

The SS-OCT/OMAG system provided high resolution cross-sectional imaging of the retina through the entire depth of the ONH, as well as the retina, choroid, and outer choroid (including the sclera and beyond) at 10 mmHg IOP (Fig. 3(a)). With the strong light scattering from the RPE and dense choriocapillaris, the choroid appears the brightest in both the structural (Fig. 3(a)) and blood flow cross-sectional images (Fig. 3(b)). An overlay of the structure and blood flow is shown in Fig. 3(c) to facilitate identification of blood flow distribution in the different posterior layers. The dashed lines in Fig. 3(c) delineate the anterior surface of the retina, the RPE and the boundary between the choroidal and outer choroidal layers which were determined by the semi-automated segmentation program. As shown in Fig. 3(d-f), we generated the blood perfusion maps for the retinal layer, choroidal layer and outer choroidal layer from the 3-D OMAG datasets, respectively. The false color represents the vessel location in 3D depth position, so the blood vessel networks in the superficial and deeper layers can be further differentiated in these images. It should be noted that, due to the strong projection tail artifacts from the blood perfusion in the retinal and choroidal layers, the true arteries and veins in the outer choroidal layer might be hidden in Fig. 3(f), which will require future effort to resolve.

The vascular perfusion demonstrated dramatic changes with progressive increases in IOP. Figure 4 shows representative OCT/OMAG images captured from the same animal in Fig. 3 at a single, selected higher IOP (80 mmHg). This demonstrates the cross-sectional structure and blood flow images from two selected B-frames: one set passing through the ONH (Fig. 4(a)-(c)), and the other more peripheral to the ONH (Fig. 4(d)-(f)). Compared to Fig.3, the structural image in Fig. 4(a), indicates posterior bowing of the retina and choroidal tissue adjacent to the ONH, and posterior displacement of the central retina artery (CRA). Judging from both flow cross-sectional images peripheral to the ONH (Fig. 4(e), (f)) and the *en face* retina image (Fig. 4(g)), the arteries and veins in the retinal layer still have good intensity signal, while the capillary network in the retinal layer is diminished at this level of IOP. In addition, choroidal blood perfusion is strongly affected, with reduced flow (Fig. 4(h)). Interestingly, a large non-perfusion zone in the choroidal layer is now evident around the ONH. More importantly, the increased IOP reduces retinal and choroidal vascular filling, which reduces light scattering by blood flow within these two layers, leading to enhanced visualization of blood vessels in the outer choroidal layers. As a result, arteries posterior to the choroid, including the arterial blood supply to the ONH at the scleral opening, such as the circle of Zinn-Haller, are now clearly visible (Fig. 4(i)).

At even higher IOPs, retinal and choroidal perfusion drastically diminishes, and is eliminated at 100 mmHg (Fig. 5). As shown in the structure cross-sectional image (Fig. 5(a)), there is severe posterior bowing of the retina and choroid around the ONH and the CRA recedes into Bruch's membrane opening. Perfusion within the retina and choroid almost entirely disappears, which can be seen in both the flow cross-sectional images (Fig. 5(b), 5(c)) and *en face* OMAG images (Fig. 5(d) and (e)). This depletion of retinal and choroidal perfusion, however, provides an excellent opportunity with less projection tail artifacts to delineate the posterior arterial supply around the ONH in and posterior to the outer choroidal layer. A complete 3-D vascular anatomy, including the circle of Zinn-Haller and the posterior ciliary arteries (PCAs), can now, for the first time, be seen *in vivo* in the rat eye (Fig. 5(f)). The reason for such visualization may be due to that these vessel structures are located outside the sclera where the IOP changes would have minimal effect.

To better evaluate the effects of elevated IOP on retinal and choroidal perfusion change, VADs for the retina and choroid, respectively, were evaluated and correlated with alterations of IOP and ocular perfusion pressure (OPP) (Fig. 6). Note that before the VAD evaluation, the flow projection artifacts within the choroid due to overlying retinal vessels were first removed using an algorithm described in [40]. At each IOP level (10 mmHg increments), the mean value of relative VAD (compared to 10 mmHg baseline) and the corresponding s.t.d (standard deviation of the mean) in 15 animals were shown and compared between the retina and choroid (Fig. 6(a)). At progressively higher IOPs, the retinal VAD dropped to 50% of baseline at 60 mmHg, whereas the choroidal VAD did not reach 50% of baseline until 70 mmHg. Using a two-tailed t-test to compare the retinal VAD relative to that of the choroid, (Fig. 6(a)), there was no statistically significant difference between retinal and choroidal relative VADs at either lower IOPs (from 10 to 40 mmHg) or the highest IOPs (from 90 to 100 mmHg). In the mid-range IOPs, the significances were $p< 0.05$ at 50, 70, 80 mmHg and $p<0.01$ at 60 mmHg, indicating that the reduction of the relative VAD in the choroid was significantly delayed compared to that in the retina. We also plotted relative VAD values at each OPP level for all animals (n=15). Sigmoidal lines best described the relationship between relative VAD and OPP for the retina as well as the choroid (Fig. 6(b)). This analysis showed that a less than 20% reduction in capillary filling density was observed as long as OPP was greater than 40 mmHg PP. At PP 40 mmHg and below, perfusion density drastically dropped in both the retina and choroid, but the choroidal curve showed a slight shift to the right, indicating the steepest reduction in perfusion began at a lower OPP, or higher IOP, than that of the retina).

4. Discussion

IOP is a well-known risk factor in glaucoma that significantly affects the perfusion to the retina and ONH, which may contribute to the development of optic nerve damage in some glaucoma patients [41]. In a portion of glaucoma patients, however, disrupted ocular perfusion and ONH blood flow have been detected without significant IOP elevation, e.g. normal tension glaucoma [42]. Unless perfusion of all the posterior vascular beds of the eye can be clearly determined in IOP models, it is difficult to establish with certainty the role of elevated IOP and ischemia in glaucomatous optic nerve damage and vision impairment. For these reasons, improving non-invasive imaging methods and measuring flow in the retina,

choroid, as well as ONH supplying arteries are important for glaucoma research and clinical care.

In our previous work, we have explored the use of SD-OCT with a SLD light source centered at either 800 nm [15] or 1300 nm [13] to study ocular structure and perfusion change in response to elevated IOP in the rat eye. The results suggested that the 1300 nm wavelength light can provide deeper penetration of ocular tissues in rodents compared to a 800 nm wavelength light, allowing for the visualization of optic disc structure at the retinal and choroidal levels with an axial resolution of −7 μm up to a depth of up to 250 μm [13]. With a 1300nm OCT system, the anatomic relationships between the ONH and surrounding posterior structure and vasculature, as well as their changes in response to elevated IOP were investigated, revealing features of posterior movement of the ONH surface and compression of the CRA at higher IOP [13]. These observations were consistent with those from other research groups using SD-OCT in rat eye IOP studies [43]. However, none of these studies provided the capability of seeing deeper than the choroid, whereas the circle of Zinn-Haller and posterior ciliary vessels, positioned behind the scleral canal opening and important for supplying blood to the retina and ONH, remained inaccessible *in vivo.* The visualization of their perfusion and changes with IOP elevation is critically important to understand ONH perfusion and vascular mechanisms of glaucomatous optic neuropathy [44].

In the current study, we used SS-OCT to perform OCT/OMAG. The SS-OCT provides long-range imaging capability and minimal sensitivity fall-off along the axial depth (Fig. 2). This improved the ability to reveal structure and blood flow through the entire thickness, including the surrounding retina, choroid and outer choroid. In addition to observing posterior bowing and shifting of the ONH and CRA (Fig. 4(a), 5(a)), the arterial blood supply to the ONH at the scleral opening could be clearly delineated *in vivo* for the first time. At the baseline IOP (10mmHg), the relative location of posterior ciliary arteries (PCAs) can be just barely seen posterior to the dense blood flow of the retina and choroid (vaguely in blue, Fig 3(f)). As IOP continued to increase and vascular filling decreased in the retina and choroid, the shape of the circle of Zinn-Haller started to appear (Fig. 4(i)), with a complete appearance at 100 mmHg along with to the PCAs (Fig. 5(f)). These vascular images at the deeper choroidal layer and beyond provide striking *in vivo* corroboration of prior findings of basic anatomic features of ONH in the rat that, until now, were only seen with *ex vivo* histological methods such as vascular casting [44]. Due to the low visibility of these vascular structures at lower IOP, caused by the multiple scattering of retinal and choroidal blood flow, however, we could not establish that these posterior vessels were unaffected by IOP elevation, but were able to confirm that perfusion to circle of Zinn-Haller and posterior ciliary vessels, located outside of the sclera, was preserved at acutely elevated IOP, including 100 mmHg.

In addition to these anatomic relationships, our ultra-high sensitive OMAG algorithm also provides dynamic monitoring of the microvascular filling in response to the elevated IOP. Previous studies using SD-OCT/OMAG have quantitatively evaluated flow filling reduction in both retinal and choroidal layers [13]. The flow reduction in retinal vessels had generally good agreement with the results reported by SD-OCT [43] and laser Doppler flowmetry [45], which is that a significant attenuation of the retinal vessels occurred when IOP was

raised to between 60~70 mmHg. Quantification of choroidal filling, however, has previously been difficult. The choroidal microvasculature is dominated by the vascular beds of the choroid and choriocapillaris that are small, dense and difficult to discriminate. Because of the sensitivity fall-off along the depth in SD-OCT, the choroidal blood flow observed by this technique appeared as a generalized, uniform signal, where blood flow in individual vessels could not be determined as well as in the retina. As a result, the filling quantification showed that the choroidal “perfusion” remained stable over a surprisingly wide range of IOPs, and only began to deteriorate noticeably at 60 mmHg, when retinal perfusion began to significantly reduce, and rapidly drop beyond this level [13]. Despite these results, the poor resolution choroidal perfusion maps used for filling quantification was not optimal for assessing the choroidal autoregulation to IOP change.

In this study, the combination of SS-OCT and an advanced ED-OMAG algorithm provides high resolution perfusion maps at both retinal and choroidal layers with a wide FOV (2.5 × 2.5 mm^2) for an improved flow quantification within the choroid. Even at the baseline IOP (10 mmHg), the vasculature in the choroid could be identified (Fig. 3(e)). With the wide FOV capability of the high-resolution choroid angiogram, we also discovered, at higher IOP (80 mmHg), a drop in choroidal vessel filling around the ONH (Fig. 4(h)). This drop-out was consistently observed in all animals in this study. However, in some of these animals, choroidal perfusion peripheral to the ONH was sustained even until 100 mHg. This discovery may have significant implications for both quantification and pathophysiology. For quantification, the peripheral perfusion was most likely missed at higher IOPs in the earlier studies using SD-OCT with the 1 × 1 mm^2 FOV at the ONH, and VAD values for the choroid would have been close to zero earlier than it would reach at a later IOP. This also explained, at least in part, why our choroidal VAD reached 50% of its baseline at a higher IOP as compared to the retinal VAD (Fig. 5). The explanation of this loss in choroidal filling immediately around the ONH, while such a pattern is not observed in the retina, remains to be explored.

It is important to note that, in this study, we observed a dramatic drop in retinal perfusion beginning at an IOP of 60 mmHg, whereas, in a prior study, this occurred at a higher pressure (around 70 mmHg) [15]. This discrepancy may be partially attributed to the much younger animals used in the present work (2 months old, ~200g vs 5~6 months old, ~300g). Fortunately, we recorded the MAP of each animal in both studies. The MAP of rats under isoflurane anesthesia was 102±4 mmHg (n=10) in the previous study, while that of younger rats in the current study, also under isoflurane, was 88±11 mmHg (n=15). Since we also compared the VAD change relative to OPP, the findings of OPP effects on vessel filling were consistent across both studies, in that greater changes in retinal filling were only observed as OPP dropped to 40 mmHg and below (Fig. 6(b)).

Currently, we have not measured blood flow directly within the ONH, while we did so in our previous SD-OCT study. As encountered in previous work, ONH perfusion signals were affected by shadowing and tailing effects caused by major overlying retinal vessels, especially at lower IOP when these vessels were fully perfused. We are currently working on approaches to minimize the impact of these shadowing effects by evaluating retinal blood flow volume and measuring ONH perfusion in response to elevation of IOP.

It is worth mentioning an additional benefit of the SS-OCT system developed in this study, which is its potential to serve as an all-in-one, versatile ophthalmic system for comprehensive assessment of the entire rodent eye, including both anterior and posterior segments. By modifying the optics in the sample arm (Figure 1), the imaging mode can be simply switched to anterior segment imaging or full eye imaging. Figure 7(a) is a structural *en face* MIP of the rat eye with a FOV of 18 × 18 mm^2, where the diameter and area size of the pupil can be measured, which might be useful in the investigation of light-stimulation studies. Figure 7(b) is a representative cross-sectional image at the middle of the eye. The internal visualization enables clear identification of the ocular structures, including the cornea, anterior chamber, iris, lens, vitreous body and retina. Figure 7(c) is the corresponding 3D rendering, which may be useful to better understand the structure of the entire eye. The A-line profile shown in Fig. 7(d) depicts the depth position of the cornea, lens and retina, enabling accurate measurement of intraocular distances, such as corneal thickness, anterior chamber depth and axial length of the eye. Since subtle malfunction of any of these structures may cause loss of vision, it may be of great clinical value to have such a comprehensive examination provided by the long-range SS-OCT system.

5. Conclusion

In summary, we have developed a new SS-OCT system operating at 1300 nm, specifically designed for evaluating ocular structure and perfusion changes in response to IOP elevation in rat eye. The excellent sensitivity fall-off performance of SS-OCT enables structural and blood flow imaging of the retina, choroid, and outer choroid, and, at higher IOPs, is capable of providing previously unattainable *in vivo* images of vascular perfusion of the circle of Zinn-Haller and PCAs. The state-of-art OCTA imaging combined with our ED-OMAG algorithm achieved high-resolution angiograms of both the retina and choroid, which enabled improved quantification of choroidal vessel filling. We believe the powerful combination of SS-OCT and OMAG in rodent models will benefit the studies of glaucoma as well as many other ocular diseases.

Acknowledgments

This work was supported in part by grants from the National Heart, Lung, and Blood Institute (R01HL093140), the National Eye Institute (R01EY024158, R01EY028753, and R01EY010145), an unrestricted grant from the Research to Prevent Blindness, Inc., and Washington Research Foundation. The funding organization had no role in the design or conduct of this research.

References

1. Flammer J, Orgül S, Costa VP, Orzalesi N, Krieglstein GK, Serra LM, Renard J-P, and Stefánsson E, "The impact of ocular blood flow in glaucoma," Prog Retin Eye Res 21, 359–393 (2002). [PubMed: 12150988]
2. Grieshaber MC and Flammer J, "Blood flow in glaucoma," Current opinion in ophthalmology 16, 79–83 (2005). [PubMed: 15744136]
3. Liang Y, Downs JC, Fortune B, Cull G, Cioffi GA, and Wang L, "Impact of systemic blood pressure on the relationship between intraocular pressure and blood flow in the optic nerve head of nonhuman primates," Investigative ophthalmology & visual science 50, 2154–2160 (2009). [PubMed: 19074806]

4. Morrison JC, Johnson EC, Cepurna W, and Jia L, "Understanding mechanisms of pressure-induced optic nerve damage," Prog Retin Eye Res 24, 217–240 (2005). [PubMed: 15610974]
5. Huang D, Swanson EA, Lin CP, Schuman JS, Stinson WG, Chang W, Hee MR, Flotte T, Gregory K, Puliafito CA, and Fujimoto JG, "Optical Coherence Tomography," Science 254, 1178–1181 (1991). [PubMed: 1957169]
6. Tomlins PH and Wang R, "Theory, developments and applications of optical coherence tomography," J. Phys. D: Appl. Phys. 38, 2519 (2005).
7. Chen CL, and Wang RK. “Optical Coherence Tomography Based Angiography.” Biomedical Optics Express 8(2): 1056–1082 (2017). [PubMed: 28271003]
8. Kashani AH, Chen CL, Gahm JK, Zheng F, Richter GM, Rosenfeld PJ, Shi Y, and Wang RK. “Optical coherence tomography angiography: A comprehensive review of current methods and clinical applications.” Progress in Retinal and Eye Research 60: 66–100 (2017). [PubMed: 28760677]
9. Zhang A, Zhang Q, Chen CL, Wang RK. “Methods and algorithms for optical coherence tomography-based angiography: a review and comparison.” J. Biomed. Opt. 20 (10), 100901 (2015). [PubMed: 26473588]
10. Wang RK. “Optical microangiography: a label-free 3-D imaging technology to visualize and quantify blood circulations within tissue beds in vivo.” IEEE J Sel. Top. Quantum Electron. 16 (3), 545–554 (2010). [PubMed: 20657761]
11. Wang RK, Jacques SL, Ma Z, Hurst S, Hanson SR, and Gruber A, "Three dimensional optical angiography," Opt. Express 15, 4083–4097 (2007). [PubMed: 19532651]
12. Wang RK, An L, Francis P, Wilson DJ. “Depth-resolved imaging of capillary networks in retina and choroid using ultrahigh sensitive optical microangiography.” Opt Lett. 35:1467–1469 (2010). [PubMed: 20436605]
13. Zhi Z, Cepurna WO, Johnson EC, Morrison JC, and Wang RK, "Impact of intraocular pressure on changes of blood flow in the retina, choroid, and optic nerve head in rats investigated by optical microangiography," Biomed. Opt. Express 3, 2220–2233 (2012). [PubMed: 23024915]
14. Zhi Z, Yin X, Dziennis S, Wietecha T, Hudkins KL, Alpers CE, and Wang RK, "Optical microangiography of retina and choroid and measurement of total retinal blood flow in mice," Biomed. Opt. Express 3, 2976–2986 (2012). [PubMed: 23162733]
15. Zhi Z, Cepurna W, Johnson E, Jayaram H, Morrison J, and Wang RK, "Evaluation of the effect of elevated intraocular pressure and reduced ocular perfusion pressure on retinal capillary bed filling and total retinal blood flow in rats by OMAG/OCT," Microvasc. Res 101, 86–95 (2015). [PubMed: 26186381]
16. Xu J, Song S, Men S, and Wang RK, "Long ranging swept-source optical coherence tomography-based angiography outperforms its spectral-domain counterpart in imaging human skin microcirculations," J. Biomed. Opt. 22, 116007 (2017).
17. Grulkowski I, Liu JJ, Potsaid B, Jayaraman V, Lu CD, Jiang J, Cable AE, Duker JS, and Fujimoto JG, "Retinal, anterior segment and full eye imaging using ultrahigh speed swept source OCT with vertical-cavity surface emitting lasers," Biomed. Opt. Express 3, 2733–2751 (2012). [PubMed: 23162712]
18. Lexer F. Hitzenberger CK, Fercher A, and Kulhavy M. "Wavelength-tuning interferometry of intraocular distances." Appl. Opt. 36, 6548–6553 (1997). [PubMed: 18259516]
19. Chinn S. Swanson E, and Fujimoto J, "Optical coherence tomography using a frequency-tunable optical source." Opt. Lett. 22, 340–342(1997). [PubMed: 18183195]
20. Oh WY. Vakoc BJ. Shishkov M. Tearney GJ. and Bouma BE. "> 400 kHz repetition rate wavelength-swept laser and application to high-speed optical frequency domain imaging." Opt. Lett. 35, 2919–2921 (2010). [PubMed: 20808369]
21. Huber R. Wojtkowski M. and Fujimoto JG. "Fourier Domain Mode Locking (FDML): A new laser operating regime and applications for optical coherence tomography." Opt. Express 14, 3225–3237 (2006). [PubMed: 19516464]
22. Bonesi M. Minneman MP. Ensher J. Zabihian B. Sattmann H. Boschert P. Hoover E. Leitgeb RA. Crawford M, and Drexler W, "Akinetic all-semiconductor programmable swept-source at 1550 nm

and 1310 nm with centimeters coherence length." Opt. Express 22, 2632–2655 (2014). [PubMed: 24663556]

23. Tsai TH. Potsaid B. Tao YK. Jayaraman V. Jiang J. Heim PJS. Kraus MF. Zhou C. Hornegger J. Mashimo H. Cable AE, and Fujimoto JG. "Ultrahigh speed endoscopic optical coherence tomography using micromotor imaging catheter and VCSEL technology." Biomed. Opt. Express 4, 1119–1132 (2013). [PubMed: 23847737]
24. Wieser W. Biedermann BR. Klein T. Eigenwillig CM. and Huber R. "Multi-Megahertz OCT: High quality 3D imaging at 20 million A-scans and 4.5 GVoxels per second." Opt. Express 18, 14685–14704 (2010). [PubMed: 20639955]
25. Xu J. Zhang C. Xu J. Wong K, and Tsia K. "Megahertz all-optical swept-source optical coherence tomography based on broadband amplified optical time-stretch." Opt. Lett. 39, 622–625 (2014). [PubMed: 24487881]
26. Xu J. Wei X. Yu L. Zhang C. Xu J. Wong K, and Tsia KK. "High-performance multi-megahertz optical coherence tomography based on amplified optical time-stretch." Biomed. Opt. Express 6, 1340–1350 (2015). [PubMed: 25909017]
27. Fechtig DJ. Grajciar B. Schmoll T. Blatter C. Werkmeister RM. Drexler W. and Leitgeb RA. "Line-field parallel swept source MHz OCT for structural and functional retinal imaging." Biomed. Opt. Express 6, 716–735 (2015). [PubMed: 25798298]
28. Tozburun S. Siddiqui M. and Vakoc BJ. "A rapid, dispersion-based wavelength-stepped and wavelength-swept laser for optical coherence tomography." Opt. Express 22, 3414–3424 (2014). [PubMed: 24663631]
29. Kang J. Feng P. Wei X. Lam EY. Tsia KK. and Wong KK. "102-nm, 44.5-MHz inertial-free swept source by mode-locked fiber laser and time stretch technique for optical coherence tomography." Opt. Express 26, 4370–4381 (2018). [PubMed: 29475287]
30. Song SZ. Xu JJ. and Wang RKK. "Long-range and wide field of view optical coherence tomography for in vivo 3D imaging of large volume object based on akinetic programmable swept source." Biomed. Opt. Express 7, 4734–4748 (2016). [PubMed: 27896012]
31. Wang Z. Potsaid B. Chen L. Doerr C. Lee H-C. Nielson T. Jayaraman V. Cable AE. Swanson E, and Fujimoto JG. "Cubic meter volume optical coherence tomography." Optica 3, 1496–1503 (2016). [PubMed: 28239628]
32. Morrison JC. Cepurna WO. Tehrani S. Choe TE. Jayaram H. Lozano DC. Fortune B, and Johnson EC. "A period of controlled elevation of IOP (CEI) produces the specific gene expression responses and focal injury pattern of experimental rat glaucoma." Investigative ophthalmology & visual science 57, 6700–6711 (2016). [PubMed: 27942722]
33. Wang RK. Xu X. He Y. Elder JB. “Investigation of optical clearing of gastric tissue immersed with hyperosmotic agents.” IEEE J.Sel. Top. Quantum Electron. 9 (2). 234–242 (2003).
34. An L. Qin J. and Wang RK. "Ultrahigh sensitive optical microangiography for in vivo imaging of microcirculations within human skin tissue beds." Opt. Express 18, 8220–8228 (2010). [PubMed: 20588668]
35. Yousefi S, Zhi ZW, and Wang RKK. "Eigendecomposition-Based Clutter Filtering Technique for Optical Microangiography." IEEE Trans. Biomed. Eng. 58(8). 2316–2323 (2011).
36. Zhang Q. Wang J, and Wang RK. "Highly efficient eigen decomposition based statistical optical microangiography." Quantitative imaging in medicine and surgery 6, 557 (2016). [PubMed: 27942476]
37. Yin X. Chao JR, and Wang RK. "User-guided segmentation for volumetric retinal optical coherence tomography images." J. Biomed. Opt. 19, 086020–086020 (2014). [PubMed: 25147962]
38. Reif R. Qin J. An L. Zhi Z. Dziennis S. and Wang R. "Quantifying optical microangiography images obtained from a spectral domain optical coherence tomography system." Journal of Biomedical Imaging 2012, 9 (2012).
39. Chu ZD. Lin J. Gao C. Xin C. Zhang QQ. Chen CL. Roisman L. Gregori G. Rosenfeld PJ. and Wang RKK."Quantitative assessment of the retinal microvasculature using optical coherence tomography angiography." J. Biomed. Opt. 21(2016).

40. Zhang AQ. Zhang QQ, and Wang RK. "Minimizing projection artifacts for accurate presentation of choroidal neovascularization in OCT micro-angiography." Biomed. Opt. Express 6, 4130–4143 (2015). [PubMed: 26504660]

41. Weigert G. Findl O. Luksch A. Rainer G. Kiss B. Vass C. and Schmetterer L. "Effects of moderate changes in intraocular pressure on ocular hemodynamics in patients with primary open-angle glaucoma and healthy controls." Ophthalmology 112, 1337–1342 (2005). [PubMed: 16024084]

42. He Z. Vingrys AJ, Armitage JA. and Bui BV. "The role of blood pressure in glaucoma." Clinical and Experimental Optometry 94133–149(2011). [PubMed: 21255075]

43. Fortune B. Choe TE. Reynaud J. Hardin C. Cull GA. Burgoyne CF. and Wang L. "Deformation of the rodent optic nerve head and peripapillary structures during acute intraocular pressure elevation." Investigative ophthalmology & visual science 52, 6651–6661 (2011). [PubMed: 21730343]

44. Morrison JC. Johnson EC. Cepurna WO. and Funk RH. "Microvasculature of the rat optic nerve head." Investigative ophthalmology & visual science 40, 1702–1709 (1999). [PubMed: 10393039]

45. He Z. Nguyen CT. Armitage JA. Vingrys AJ. and Bui BV. "Blood pressure modifies retinal susceptibility to intraocular pressure elevation." PLoS One 7, e31104 (2012). [PubMed: 22359566]

Highlights

- 1300nm swept-source optical coherence tomography (SS-OCT) system offers superb ability to image rodent eyes with enhanced imaging depth beyond sclera tissue and is useful in evaluating the effects of intraocular pressure (IOP) elevation on ocular circulation.
- The SS-OCT provides structural and blood flow imaging of the retina, choroid, and outer choroid, and, at higher intraocular pressures, is capable of providing previously unattainable in vivo images of vascular perfusion of the circle of Zinn-Haller and PCAs.

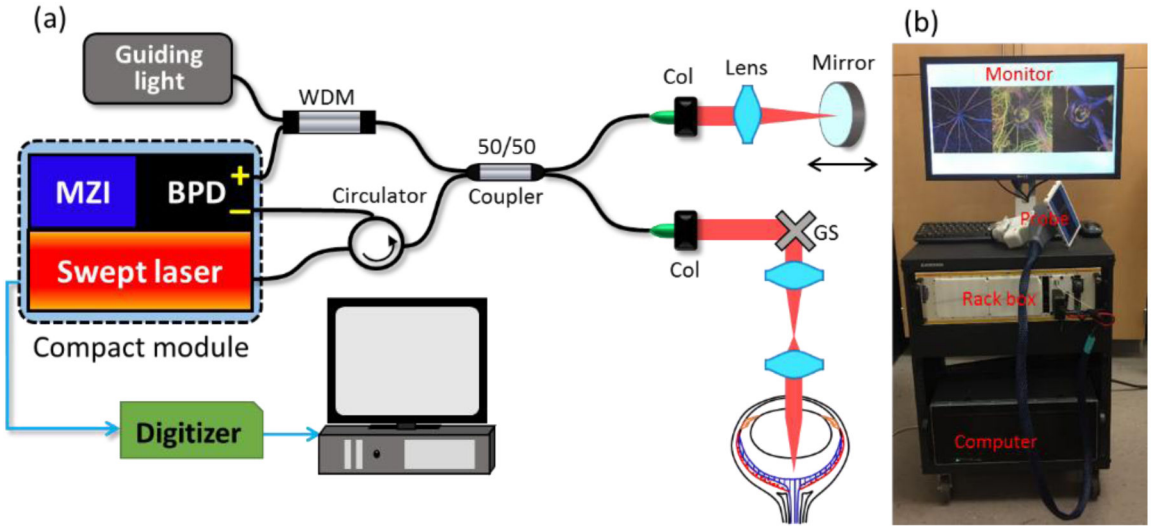

Fig. 1.

(a) Schematics of the SS-OCT setup for *in vivo* rat eye imaging. BPD: balanced photodetector, MZI: Mach-Zehnder interferometer, WDM: wavelength division multiplexer, Col: collimator, GS: galvo scanner. (b) Photograph of the compact SS-OCT system.

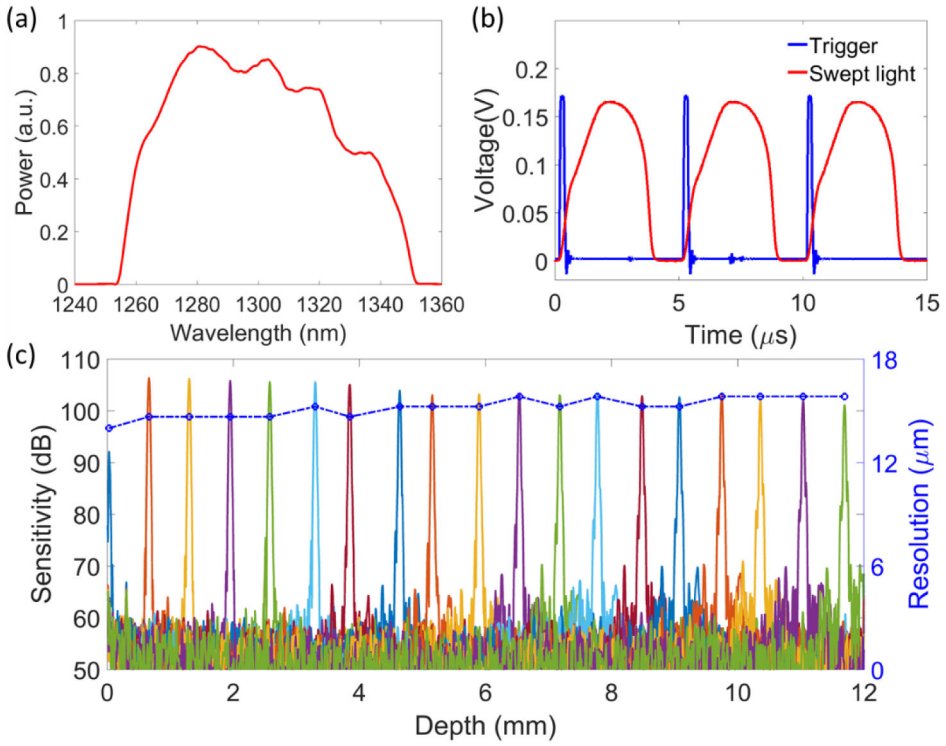

Fig. 2.

(a) Spectrum of the swept laser. (b) Signals of laser trigger (blue) and swept light waveform (red). (c) The sensitivity fall-off curves and the axial resolutions measured at different depth positions. The blue line indicates the measured axial resolution along the ranging distance.

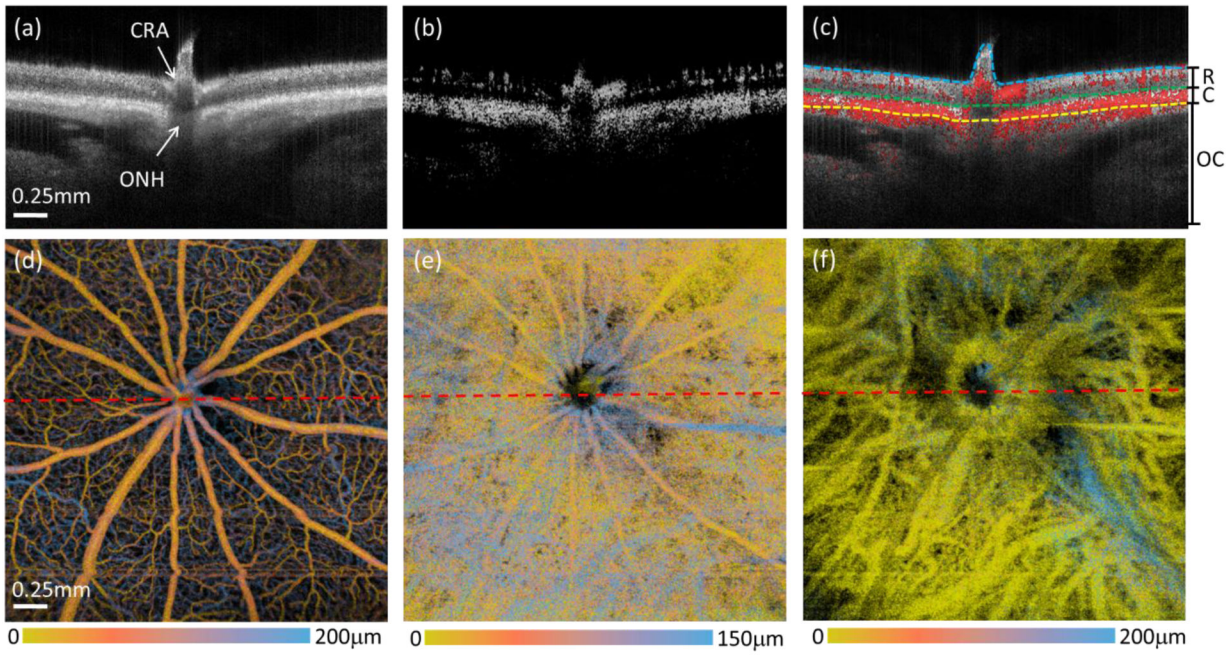

Fig. 3.

OCT/OMAG provides structure and blood flow perfusion information of the entire posterior segment of the rat eye at 10 mmHg IOP. (a-c) are the cross-sectional images of the structure (a), blood flow (b), and their overlay (c). The dashed lines in (c) are segmentation lines that depict the anterior surface of retina (cyan), the RPE (green) and the boundary between the choroid and outer choroid (yellow). (d-f) are false color *en face* MIPs of the blood flow in the retina, choroid and outer choroid, respectively. The color bars indicate the depth-encoded color with the depth measured from the top of the slab that was used to produce the blood perfusion maps as shown. The red dashed lines in (d-f) indicate the position of the cross-sectional images shown in the top row. CRA: central retinal artery, ONH: optic nerve head, R: retina, C: choroid, OC: outer choroid.

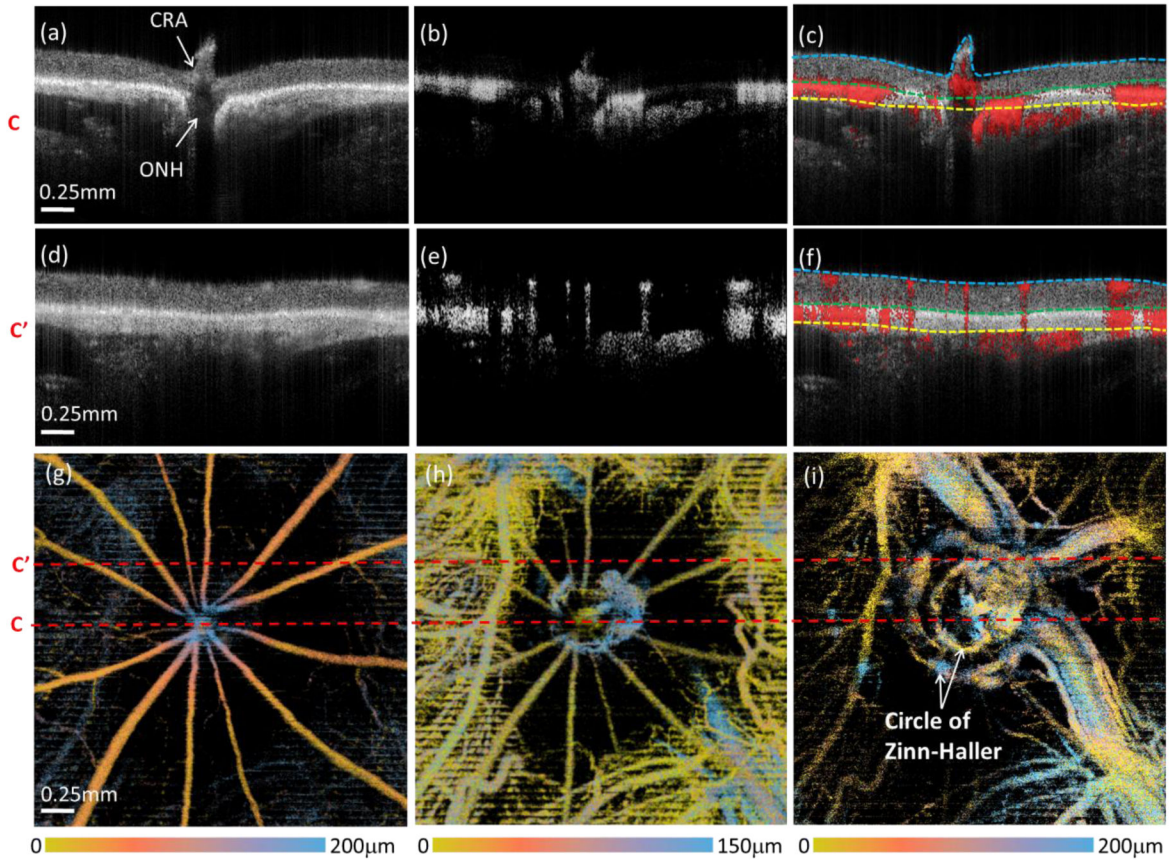

Fig. 4.

OCT/OMAG enables clear visualization of the structure and perfusion information of the posterior segment of the rat eye at 80 mmHg IOP. (a-f) are the cross-sectional images of the structure (left), blood flow (middle), and their overlay (right). (a-c) are the cross-sectional images going through ONH, and (d-f) are peripheral to ONH. The dashed lines in (c) and (f) are segmentation lines that depict the anterior surface of retina (cyan), the RPE (green) and the boundary between choroid and outer choroid (yellow). (g-i) are false color *en face* MIPs of the blood vessels in the layer of retina, choroid and outer choroid, respectively. The color bars indicate the depth-encoded color with the depth measured from the top of the slab that was used to produce the blood perfusion maps as shown. The red dashed lines in (g-i) indicate the position of the cross-sectional images shown above. CRA: central retinal artery, ONH: optic nerve head.

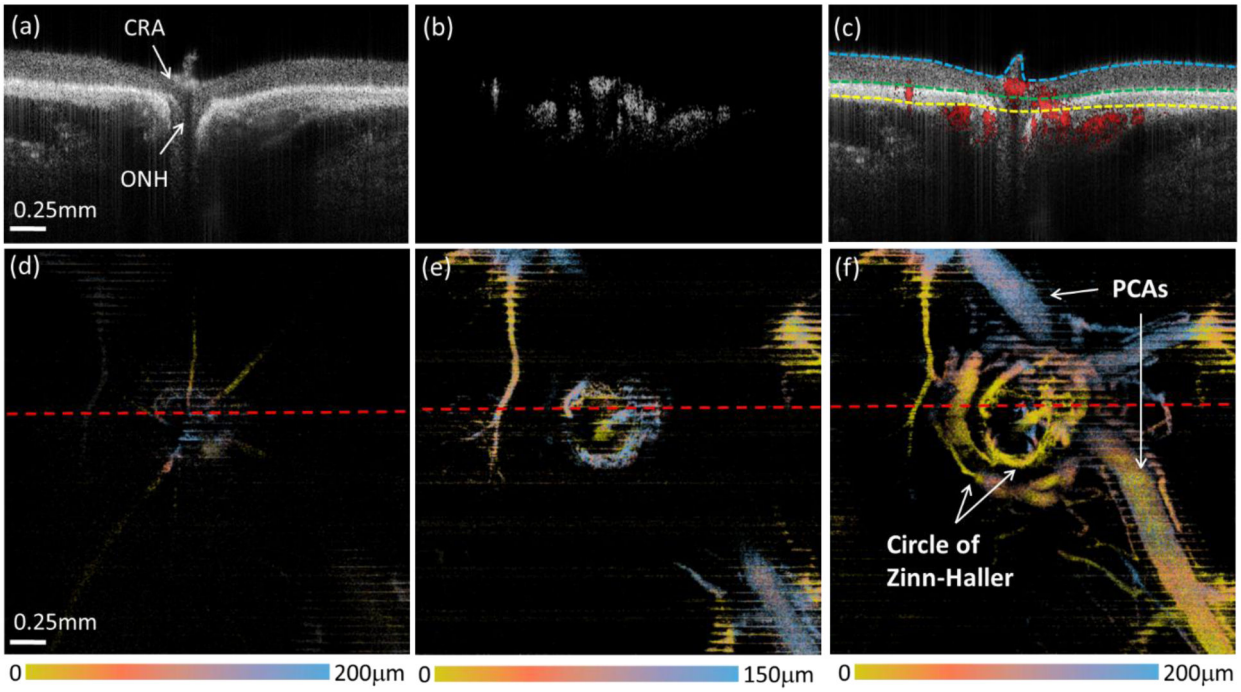

Fig. 5.

Reduction in perfusion within the retina and choroid at 100 mmHg IOP enables complete visualization of posterior arterial supply around ONH. (a-c) are the cross-sectional images of the structure, blood flow, and their overlay, respectively. The dashed lines in (c) are segmentation lines that depict the anterior surface of retina (cyan), the RPE (green) and the boundary between choroid and outer choroid (yellow). (d-f) are false color *en face* MIPs of the blood vessels in the layer of retina, choroid and outer choroid, respectively. The color bars indicate the depth-encoded color with the depth measured from the top of the slab that was used to produce the blood perfusion maps as shown. The red dashed lines in (d-f) indicate the position of the cross-sectional images shown in the top row CRA: central retinal artery, ONH: optic nerve head, PCAs: posterior ciliary arteries.

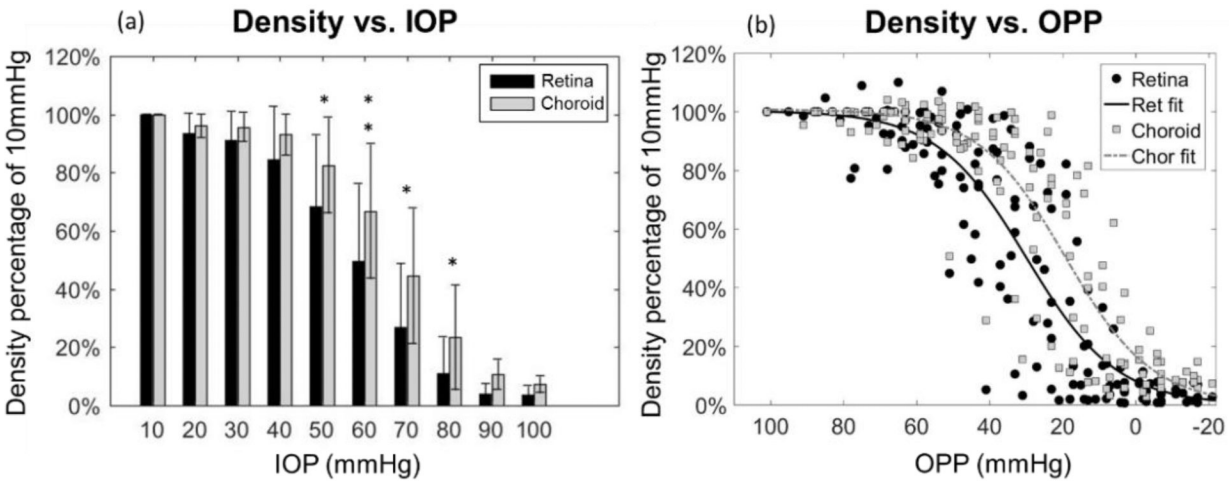

Fig. 6.

Comparison of retinal and choroid perfusion in response to the change in IOP and OPP. (a) Relative VAD (compared to 10 mmHg) in relation to increased IOP. Bar values represent mean ± s.t.d (standard deviation of the mean) for either retina or choroid. IOP levels with a significant difference between the retina and choroid are indicated by * for $P < 0.05$ and ** for $P < 0.01$. (b) Relative VAD (to 10 mmHg) in comparison to decreasing levels of OPP. The sigmoidal fitting values are R^2=0.8634 and R^2=0.8503 for retina and choroid, respectively. OPP = MAP - IOP. MAP is 88 ± 11 (n=15).

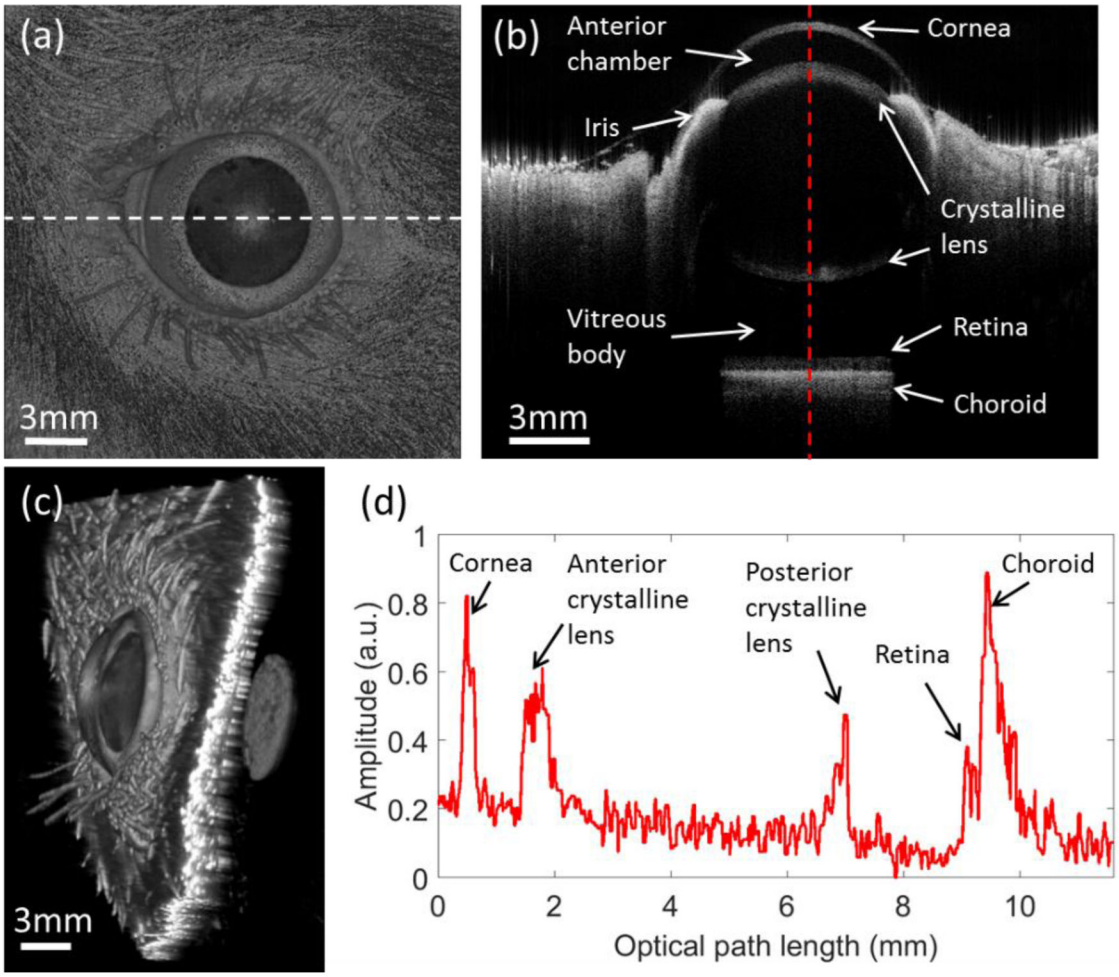

Fig. 7.

The full eye structural OCT images for the rat with a field of view 18mm × 18mm. (a) is the *en face* MIP of the 3D OCT dataset. (b) is the cross-sectional OCT images at the position indicated by the white dashed line in (a). (c) is the 3D rendering of the rat eye. (d) is the A-line profile at the position indicated by the red dashed line in (b).